Interplay between optical pumping and Rydberg EIT in magnetic fields

LINJIE ZHANG,[1,2,*] SHANXIA BAO,[1,3] HAO ZHANG,[1,2] GEORG RAITHEL,[1,5] JIANMING ZHAO,[1,2] LIANTUAN XIAO[1,2] AND SUOTANG JIA[1,2]

[1]*State Key Laboratory of Quantum Optics and Quantum Optics Devices, Institute of Laser Spectroscopy, Shanxi University, Taiyuan 030006, China*
[2]*Collaborative Innovation Center of Extreme Optics, Shanxi University, Taiyuan 030006, China*
[3]*Institute of Theoretical Physics, Shanxi Datong University, Datong 037009, Datong, China*
[4]*Department of Physics, Shanxi Datong University, Datong 037009, Datong, China*
[5]*Department of Physics, University of Michigan, Ann Arbor, MI 48109-1120, USA*
[*]*zlj@sxu.edu.cn*

Abstract: We perform Zeeman spectroscopy on a Rydberg electromagnetically induced transparency (EIT) system in a room-temperature Cs vapor cell, in magnetic fields up to 50 Gauss. The magnetic interactions of the $|6S_{1/2} F_g = 4>$ ground, $|6P_{3/2} F_e = 5>$ intermediate, and $|33S_{1/2}>$ Rydberg states that form the ladder-type EIT system are in the linear Zeeman, quadratic Zeeman, and the Paschen-Back regimes, respectively. We explain the dependence of Rydberg EIT spectra on the magnetic field and polarization. The asymmetry of the EIT spectra, which is caused by the quadratic Zeeman effect of the intermediate state, becomes paramount in magnetic fields ≥40 Gauss. We investigate the interplay between Rydberg EIT, which reduces photon scattering, and optical pumping, which relies on photon scattering. We employ a quantum Monte Carlo wave-function approach to quantitatively model the spectra and their asymmetry behavior. Simulated spectra are in good agreement with the experimental data.

1. Introduction

Rydberg atoms, highly excited atoms with principal quantum numbers $n >> 1$ [1], possess extraordinary properties, such as long lifetime and strong dipole-dipole interaction. These offer considerable potential for applications in quantum information processing [2,3], non-linear optics [4,5] and non-equilibrium phenomena [6–8]. Their strong response to microwave electric fields makes these atoms attractive for performing traceable microwave measurements [9,10]. Electromagnetically induced transparency (EIT) [11], a quantum interference effect, has been extended to ladder-type systems that include Rydberg energy levels. A. K. Mohapatra et al. introduced EIT as an optical, nondestructive method to probe Rydberg states in vapor cells [12]. Later, a giant electro-optic effect based on polarization dark states was observed [13]. C.Wade et al. demonstrated a room-temperature Terahertz detector basing on Terahertz-driven non-equilibrium phase transitions using Rydberg EIT in a thermal vapor cell [14]. Sedlacek et al. demonstrated polarization measurement of microwave electric fields in a Rydberg EIT system, accounting for 52 levels [15]. The features of Aulter-Towns splitting and EIT depend on the polarizations of the microwave electric field and the two excitation beams. In our previous work we investigated the role of the laser-field polarization in Rydberg EIT, and qualitatively modeled its Zeeman spectra using standard density matrix method [16]. The effect of optical pumping on the transmission, width and profile of EIT spectra has already been discussed in Λ and ladder-type systems [17–20]. The effect of optical pumping in diatomic molecules has been investigated [21,22]. Recently, it has been shown that the Zeeman effect and optical pumping play important roles in quantum information processing and Rydberg-atom molecules [3,23–25].

Level populations and coherences in ladder-type Rydberg EIT systems are affected by the Zeeman shifts of the magnetic sub-states of ground, intermediate and Rydberg energy levels. Linear and quadratic Zeeman splittings affect EIT line positions and optical pumping rates, and have a pronounced effect on the steady-state and dynamic behavior. The systems exhibit an interdependence between optical pumping, which scales with the photon scattering rate, and EIT, which reduces photon scattering. In vapor cells one further needs to account for a continuum of velocity classes and Doppler shifts, which add to the multitude of lines that can be simultaneously observed [26]. The observed line shapes depend on Zeeman shifts and optical pumping, with the quadratic Zeeman effect introducing strong asymmetries in the line patterns. In the present work we perform a careful analysis of these phenomena. The results are relevant in applications that involve moderate magnetic fields, in the range of tens to hundreds of Gauss, and in which Rydberg level shifts are used to diagnose other fields. Our results are, for instance, applicable to electric-field diagnostics in plasmas confined / guided by magnetic fields (process plasmas, plasma discharges, Hall thrusters etc.) [27-29].

In the present work, we study Rydberg EIT in a vapor cell in a magnetic field that is parallel to the laser-beam directions. The Rydberg EIT spectra exhibit quadratic Zeeman shifts and asymmetries that develop with increasing magnetic field, and that become significant at fields as low as a few tens of Gauss. Our study shows that these features are caused by the quadratic Zeeman effect of the $6P_{3/2}$ $F_e = 5$ levels, and by the interplay between EIT and optical pumping. We also observe EIT doublets that reflect the spin-up/spin-down structure of the Rydberg energy levels (which are deep in the hyperfine Paschen-Back regime). We employ a quantum Monte-Carlo wave-function (QMCWF) approach to model the Zeeman spectra of Rydberg EIT. Simulation results are in good agreement with our experiments and afford further insight into the optical-pumping dynamics.

2. Experimental setup

The ladder three-level system is formed by the ground state $6S_{1/2}$ ($F_g = 4$), the intermediate state $6P_{3/2}$ ($F_e = 5$) and the $33S_{1/2}$ Rydberg state of ^{133}Cs, which are denoted |g>, |e> and |r>, respectively, as shown in Fig. 1(a) (left). The experiments are performed in a room-temperature Cs vapor cell with the counter-propagating probe and coupling beams focused into the center of the cell. The experimental setup is sketched in Fig. 1(b). The laser beams propagate in the z direction (quantization axis), parallel to the magnetic field. The probe laser (DL100, Toptica) has a wavelength $\lambda_P \approx 852$ nm. The probe beam has a power of 2 μW and a $1/e^2$ waist of $\omega_0 = 130$ μm. The probe laser is locked on a high-finesse Fabry-Perot cavity with a spacer made from ultra-low thermal expansion glass (Stable Laser Systems ATF-6010-4) and has a linewidth smaller than 100 kHz. The probe laser resonantly drives the $6S_{1/2}$ ($F_g = 4$)→ $6P_{3/2}$ ($F_e = 5$) transition. The coupling laser is a frequency-doubled Toptica TA-SHG Pro system with an output wavelength $\lambda_C \approx 510$ nm. The coupling beam has a power of 20 mW, a $1/e^2$ waist of 130 μm, and a linewidth of about 1 MHz. The coupling laser is scanned through the $6P_{3/2}$ ($F_e = 5$) →$33S_{1/2}$ Rydberg-state transition. During the experiments, the probe laser is locked on-resonance, and its transmission through the atomic vapor cell is monitored while the coupling laser is scanned. In this method, there is no variation of the coupling-beam-free absorption signal, as the probe always resonantly interacts with the same velocity class in the Maxwell velocity distribution. The coupling-beam-induced EIT transmission peaks then appear on a flat background. As sketched in Fig. 1(b), the Cs vapor cell (length 4 cm and diameter 2 cm) is placed inside a much longer cylindrical solenoid (length 25 cm, inner diameter 5 cm, three layers of 211 windings each), so that the uniformity of the magnetic field along the length of the vapor cell is guaranteed. The magnetic field is set to values between 0 and 50 Gauss, with a variation of less than ± 0.1 Gauss within the cell. The solenoid is enclosed within several layers of magnetic-shielding material to eliminate the influence of environmental magnetic fields. To ensure well-defined polarizations, both the coupling and probe beams are passed through combinations of half-wave plates (λ/2), Glan-Taylor

polarizers (GTP) and quarter-wave plates (λ/4), located immediately before the beams enter the cell.
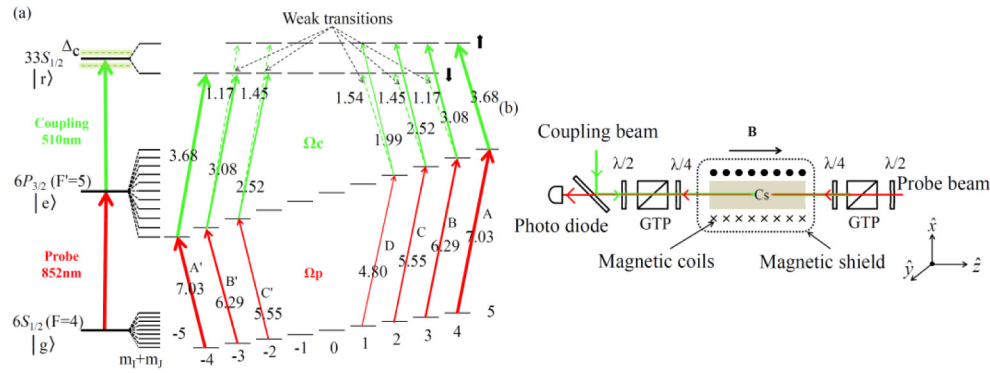

Fig. 1. (a) Energy-level scheme of cesium Rydberg EIT without (left) and with (right) magnetic field. The 852-nm probe laser is resonant with the field-free transition $6S_{1/2}$ $F_g = 4 \rightarrow 6P_{3/2}$ $F_e = 5$, and the 510-nm coupling laser scans through the $6P_{3/2}$ $F_e = 5 \rightarrow 33S_{1/2}$ Rydberg-state transition. The coupling detuning relative to the field-free transition $6P_{3/2}$ $F_e = 5 \rightarrow 33S_{1/2}$ is denoted Δ_c. The right side of the energy level scheme shows the Zeeman sublevels of the |g>, |e> and |r> states when a magnetic field on the order of ten Gauss is applied (main separations not to scale). The level ladders that lead to strong signals in the EIT spectra measured with linearly polarized fields (laser electric fields pointing along x) are labeled A, B, C, D and A′, B′, C′ (line thickness increases with line strength). The numbers show Rabi frequencies $\Omega/2\pi$ in MHz, for our experimental conditions. The stronger coupling transitions (solid green lines, Type I) approximately maintain the electron spin, while in the weaker ones (dashed green lines, Type II) the spin mostly flips. (b) Schematic of the experimental setup. The probe and coupling beams are counter-propagating and focused into the center of the cell, which is contained in a cylindrical solenoid and multi-layer magnetic shield. The indicated coordinates define magnetic-field and polarization directions. Half-wave plates (λ/2), Glan-Taylor polarizers (GTP) and quarter-wave plates (λ/4) are used for polarization control.

Considering that the thermal velocity in one dimension is 140 m/s, for the given beam diameters the effective atom-field interaction time is 1 μs. This value is important because it limits the effectiveness of optical pumping, and it is used in the theoretical model in Sec. 3 as propagation time of the quantum trajectories.

We use an auxiliary magnetic-field-free EIT reference setup (not shown), which is similar to the one sketched in Fig. 1(b) and is operated with the same lasers as the main setup. When scanning the coupling laser, the EIT spectrum from the reference cell exhibits a pair of peaks that correspond to the two magnetic-field-free cascade transitions $6S_{1/2}$ ($F_g = 4$)→$6P_{3/2}$ ($F_e = 5$)→$33S_{1/2}$ and $6S_{1/2}$ ($F_g = 4$)→$6P_{3/2}$ ($F_e = 4$) →$33S_{1/2}$. The separation between the two reference peaks is 168 MHz (i. e., the actual $6P_{3/2}$ ($F_e = 4$) to $6P_{3/2}$ ($F_e = 5$) splitting multiplied with a Doppler correction factor (λ_P/λ_C)-1) [27]. This allows us to calibrate the coupling laser frequency, and to precisely measure the absolute Zeeman splittings due to the magnetic field applied to the vapor cell. The coupling frequency at which the $6S_{1/2}$ ($F_g = 4$)→$6P_{3/2}$ ($F_e = 5$) →$33S_{1/2}$ reference peak occurs defines $\Delta_C = 0$ in the following EIT spectra.

3. Theoretical model

3.1 Hyperfine Hamiltonian and EIT resonances

In our calculations we employ the {$|m_I, m_J >$} basis, with $m_I = -7/2, -5/2, ..., 5/2, 7/2$ for ^{133}Cs and $m_J = \pm 1/2$ for |g> and |r>, and $m_J = \pm 1/2, \pm 3/2$ for |e>. In this basis, the computation of the matrix elements of the below operators is straightforward.

For an atom with velocity v in the z direction, the Doppler corrected field-free part of the total effective Hamiltonian is

$$\hat{H}_0 = -\left(\Delta_P + k_P\upsilon + \frac{i}{2}\Gamma_e\right)\hbar|e\rangle\langle e| - \left(\Delta_P + \Delta_C + (k_P - k_C)\upsilon + \frac{i}{2}\Gamma_r\right)\hbar|r\rangle\langle r|, \quad (1)$$

with probe and coupling-laser angular-frequency detunings Δ_P (fixed and ≈ 0) and Δ_C (scanned), wavenumbers k_i for $i = P, C$, intermediate-state decay rate $\Gamma_e = 2\pi \times 5.2$ MHz, and short-hands for the intermediate- and Rydberg-state projectors $|e\rangle\langle e|$ and $|r\rangle\langle r|$ (which include sums over the magnetic quantum numbers). The Rydberg-state decay rate Γ_r is negligibly small (here $\Gamma_r = 2\pi \times 10$ kHz) [1]. When solving the time-dependent Schrödinger equation, the imaginary parts of the effective Hamiltonian lead to an exponential decay of the norm of the wavefunction that is consistent with the decay rates and wave-function probabilities in $|e\rangle$ and $|r\rangle$. The wavefunction decay is important in the implementation of the quantum Monte-Carlo wave-function (QMCWF) method. The hyperfine Hamiltonian is given by

$$\hat{H}_{hfs} = \frac{A_{hfs}\hat{I}\cdot\hat{J}}{\hbar^2} + B_{hfs}\frac{\left[3(\hat{I}\cdot\hat{J})^2 + (3\hbar^2/2)(\hat{I}\cdot\hat{J}) - I(I+1)J(J+1)\right]}{2I(2I-1)J(2J-1)}, \quad (2)$$

where A_{hfs}, B_{hfs} are the magnetic dipole and electric quadrupole constants of the hyperfine structure (HFS), respectively (the magnetic octupole interaction is neglected). Values for the ground- and intermediate state hyperfine constants are taken from [30]. The electronic- and nuclear-spin operators are denoted $\hat{J}$ and $\hat{I}$, respectively. For the ground and Rydberg states $B_{hfs} = 0$. For $nS_{1/2}$ Rydberg energy levels $A_{hfs} = h \times 13.2$ GHz/$(n-\delta_S)^3$ [31], with quantum defect $\delta_S = 4.05$. For $33S_{1/2}$, the Rydberg state used in this work, the energy separation of the field-free $F_r = 3$ and $F_r = 4$ HFS states is only about $h \times 2$MHz. In the magnetic-field range studied and at the present level of precision, which is limited by the EIT linewidth, this Rydberg HFS is negligible.

Table 1. Sketch of the total Hamiltonian of our ladder-type system.

$|r\rangle$	$|e\rangle$	$|g\rangle$
$nS_{1/2}$ B	Ω_C	0
Ω_C	$6P_{3/2}$ B,HFS	Ω_P
0	Ω_P	$6S_{1/2}$ B,HFS

For a magnetic field B pointing in the z direction, the interaction Hamiltonian can be given by

$$\hat{H}_B = \frac{\mu_B}{\hbar}(g_J\hat{J}_z + g_I\hat{I}_z)B, \quad (3)$$

where μ_B is the Bohr magneton, and g_J and g_I are the Landé g-factor and the nuclear g-factor ($g_I \ll g_J$). The optical atom-field interactions are, in the rotating frame,

$$\hat{H}_i = E_i\varepsilon_i\cdot\hat{d}_i/2 \quad (4)$$

with field amplitudes E_i, polarization unit vectors ε_i and electric-dipole operators $\hat{d}_i$, for the probe and coupling fields $i = P$ and C, respectively. In the geometry in Fig. 1, we employ polarization unit vectors $\varepsilon_i = \hat{x}$ or $\varepsilon_i = (\hat{x} \pm i\hat{y})/\sqrt{2}$, for linear and circular polarization, respectively. The probe-laser interaction matrix elements are of the form

$\hbar\Omega_P = \hbar\Omega_{P,r}\theta^{l',J',m'_J}_{l,J,m_J}/2$, with an m-independent radial Rabi frequency $\Omega_{P,r}$ and an angular matrix element $\left\langle l',J',m'_J \left| e^{\pm i\phi}\sin\theta \right| l,J,m_J \right\rangle = \theta^{l',J',m'_J}_{l,J,m_J}$.

For instance, for the case of a σ^+-polarized probe $\left\langle e,m'_J \left| \hat{\Omega}_P \right| g,m_J \right\rangle = \delta_{m'_J,m_J+1}\Omega_{P,r}\theta^{6P_{3/2},m'_J}_{6S_{1/2},m_J}/2$. Analogous expressions apply to the coupling-laser interaction and other polarization. All optical couplings are diagonal in the nuclear magnetic quantum number m_I.

The structure of the total Hamiltonian of our ladder-type system is illustrated in Table 1. It is seen that the Hamiltonian takes a block-diagonal form. The diagonal blocks contain the hyperfine [Eq. (2)], magnetic [Eq. (3)] and field-free terms [Eq. (1)]. The decay of the system almost exclusively comes from the spontaneous emission of the $6P_{3/2}$ level, which is included in the center diagonal block. The diagonal blocks also depend on the atom velocity, as shown in [Eq. (1)]. The off-diagonal blocks contain the optical couplings [Eq. (4)], which are m_J-dependent according to the given polarization. As shown in Fig. 1(a) (right), the degeneracy of the Zeeman sublevels is lifted when the external magnetic field is applied. The figure shows the case of a weak field (about 10 Gauss). The ground levels are well within the linear Zeeman regime, in which the usual F and m_F quantum numbers are good quantum numbers. The ground-state hyperfine Landé g-factor $g_{F,g}$ equals 0.25. In Fig. 1(a) the intermediate levels are still within the linear Zeeman regime, with $g_{F,e} = 0.4$, but develop significant quadratic Zeeman effect for larger magnetic-fields. The Rydberg state is deep in the Paschen-Back regime, where F and m_F are not good quantum numbers. For |r>, all magnetic sub-states have well-defined m_J, and the nuclear magnetic moment, m_I, contributes no significant energy shift. Hence, the Rydberg states in the magnetic field have just two sets of m_I-degenerate levels, which are labeled spin-up and spin-down in Fig. 1(a). While the Zeeman shifts range from the linear (|g>) and the quadratic Zeeman (|e>) to the deep Paschen-Back regime (|r>), in our geometry the quantity $m_I + m_J$ is well-defined in all regimes. In Fig. 1(a), both probe and coupling lasers are linearly polarized in x-direction and consist in equal parts of σ^+- and σ^--components with respect to the z quantization axis (which is parallel to the magnetic field, as seen in Fig. 1). The major transitions are labeled A, B, C, D and A′, B′, C′, in analogy with the labeling used in the EIT spectra below. In Fig. 1 we indicate the Rabi frequencies $\Omega/2\pi$ at the beam centers, for a probe power of 2 μW and waist $\omega_0 = 130$ μm, and for a coupling power of 20 mW and waist $\omega_0 = 130$ μm. The transitions from intermediate states into Rydberg states are divided into strong transitions, (Type-I, green solid lines), and weak transitions (Type-II, green dashed lines). The line-strength difference results in large parts from the degree of electron spin overlap between the intermediate and Rydberg states.

The EIT line positions as a function of coupling-laser detuning, Δ_C, follow from the Zeeman shifts Δ_g, Δ_e and Δ_r of the ground, intermediate and Rydberg energy levels, and the fixed detuning of the probe laser, Δ_P. In the linear Zeeman regime, B≤10 Gauss, and for ground- and intermediate state magnetic quantum numbers $m_{F,g}$ and $m_{F,e}$, and respective hyperfine g-factors $g_{F,g} = 0.25$ and $g_{F,e} = 0.4$, the level shifts from the magnetic field-free level positions are:

$$\Delta_g = \frac{\mu_B}{\hbar}B g_{F,g} m_{F,g}$$

$$\Delta_e = \frac{\mu_B}{\hbar}B g_{F,e} m_{F,e} \tag{5}$$

$$\Delta_r = \frac{\mu_B}{\hbar}B(g_{J,r}m_J + g_I m_I) + \frac{A_{hfs,r}}{\hbar}m_I m_J$$

For the $33S_{1/2}$ Rydberg level of ^{133}Cs, the hyperfine coupling constant $A_{hfs,r}$ is only about $h \times 0.5$ MHz. Hence, the Rydberg level is deep in the Paschen-Back regime of the HFS, and

there are no apparent Rydberg HFS effects. (The Rydberg hyperfine term $A_{hfs,r} m_I m_J$ is still included in our calculations). Moreover, $g_{J,r} \approx 2.00232$ (the electron g-factor) and $g_I \sim -10^{-4} g_{J,r}$ (*i.e.*, the Rydberg-level shifts due to the nuclear magnetic moment are even less than those due to the Rydberg-HFS). As a result, there are only two relevant Rydberg energy levels, $m_J = \pm 1/2$, and they are essentially m_I-degenerate (see Fig. 1 (a)). Taking into account all hyperfine shifts and magnetic splittings of the relevant levels as a function of B [4], there is a large number of electric-dipole-coupled transitions with different detuning (see Fig. 1 (a)). For fields $B \geq 10$ Gauss the second-order Zeeman effect of the intermediate level becomes important; in this case the magnetic level shifts Δg and Δe are obtained by diagonalization of the optical-field-free Hamiltonian in the $\{|m_I, m_J\rangle\}$ basis. The EIT line positions for fixed probe detuning Δ_P are obtained by requiring resonance for both the probe and the coupling laser on a three-level ladder connected via dipole-allowed transitions. The resonance conditions are solved by treating the atom velocity v and coupling-laser detuning Δ_C as free variables. The solutions are

$$v = \frac{\lambda_P}{2\pi}\left(\Delta_P + \Delta_g - \Delta_e\right)$$

$$\Delta_C = \Delta_r + \Delta_e\left(\frac{\lambda_P}{\lambda_C} - 1\right) - (\Delta_P + \Delta_g)\frac{\lambda_P}{\lambda_C}$$

$$= \Delta_r + 0.67\Delta_e - 1.67(\Delta_P + \Delta_g)$$

(6)

with sets of detunings Δg, Δe and Δr that correspond with sets of three states that have dipole-allowed probe and coupling transitions. There are many solutions, as indicated in Fig. 1(a). For B≤10 Gauss, the detunings follow from Eq. (5). Since in much of our work the magnetic field is higher, we obtain detunings and magnetic-field-perturbed states by numerical diagonalization of $\hat{H}_{hfs} + \hat{H}_B$ (see Eqs. (2) and 3) within the respective ground-, intermediate- and Rydberg-level subspaces.

3.2. Monte-Carlo approach to model optical pumping and EIT lineshape

To interpret the rich structure that we measure in our experimental Rydberg EIT spectra in magnetic fields (multiple line positions, line strengths and line shapes), it is essential to employ a quantitative model that accounts for the exact dependence of the optical couplings on magnetic quantum numbers and beam polarization, atom decay, optical pumping among the magnetic sublevels, the nonlinear Zeeman effect, and Rydberg-level dephasing. In the geometry given in Fig. 1(b), in general all $6S_{1/2}$, $6P_{3/2}$ and $nS_{1/2}$ states are coupled to each other by the optical fields and the spontaneous decay of the excited states. For ^{133}Cs, which has $I = 7/2$, the size of the relevant Hilbert space is $N = 64$. This is sufficiently large to seek the benefits of the quantum Monte-Carlo wavefunction (QMCWF) method to determine the density matrix, rather than to directly solve the quantum Master equation. In the QMCWF approach [32,33], one generates large sets of quantum trajectories whose evolution consists of deterministic segments of Hamiltonian propagation (with a non-Hermitian effective Hamiltonian) and discrete, stochastic quantum jumps. After each quantum jump the wave-function is re-set to a new, normalized wavefunction that is consistent with the quantum measurement of a spontaneously emitted photon. The density matrix is constructed from an average over a sufficiently large sample of quantum trajectories. It has been shown that the QMCWF method is equivalent to the standard density matrix analysis [15]. If the dimension of the quantum system is large, as in the present case with $N = 64$, the number of variables in the wavefunction process ($N = 64$) is much smaller than the number of variables in the density-matrix analysis ($N^2 = 4096$), so that the QMCWF becomes numerically a better choice. The QMCWF method also extends to even larger systems, such as ones that involve D-state Rydberg energy levels (for which the dimension of the quantum system would be $N =$

128). Therefore, for our interpretation of the ^{133}Cs Rydberg EIT spectra we employ the QMCWF method. The fundamentals of the method are explained in Refs [32,33]; our own work on QMCWF in context with laser cooling in a variety of optical lattices is summarized in [34] and references therein. In the present work, we use the QMCWF to obtain the probe-photon scattering rate per atom on a grid of atom velocities v in the cell and over a range of the coupling laser detuning Δ_C, for selected values of the magnetic field B and radial Rabi frequencies, $\Omega_{P,r}$ and $\Omega_{C,r}$, and for the laser polarization we have investigated in the experiment. As sufficiently large atom samples we typically use 2000 quantum trajectories integrated over 1 µs each. The propagation time has been chosen to be 1 µs because the atom-field interaction time in the cell is on that order (see Sec. 2). We also have allowed for a Rydberg-collision-induced phase diffusion of the Rydberg-state part of the quantum trajectories; the Rydberg phase diffusion rate used is 1.8×10^6 s^{-1}, corresponding to an average phase change of about $\pi/2$ over the interaction time.
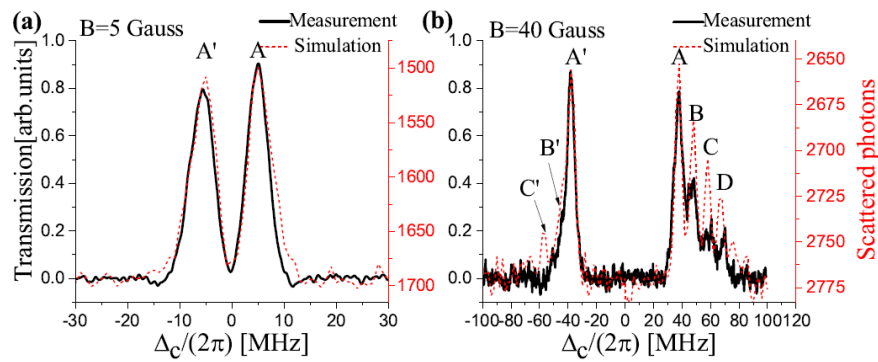

Fig. 2. Measurements (left axes, black solid lines) and simulations (right axes, red dashed lines) of Rydberg EIT spectra with magnetic fields of 5 Gauss (a) and 40 Gauss (b). The probe and coupling beams are both linearly polarized in x-direction (transverse to the magnetic field). The experimental data show an increase in transmission above its coupling-laser-free value. EIT on the various three-level ladder systems identified in Fig. 1(a) results in several peaks. The QMCWF simulations show the number of photons scattered by a typical atom sample in the cell (note the number of scattered photons is plotted in descending direction). EIT corresponds with a reduction in photon scattering. With increasing magnetic field, the Rydberg EIT line splits into two approximately symmetric main peaks A′ and A. Asymmetric satellite lines, labeled B′, C′ and B, C, D, appear outside of the interval between A′ and A. The peak labels correspond to the transition labels in Fig. 1(a).

4. Experimental spectra of Rydberg EIT in magnetic field

4.1 Magnetic-field-induced EIT line asymmetry

Figures 2(a) and 2(b) show experimental Rydberg EIT spectra in axial magnetic fields of $B = $ 5 Gauss and 40 Gauss, respectively, as well as the results of corresponding QMCWF simulations. The probe and coupling beams are both linearly polarized in x-direction. The intrinsic EIT linewidth is ~8 MHz; it is mostly due to power broadening on the probe and coupling transitions as well as residual laser linewidth effects. In Fig. 2(a) we mostly see a peak height difference on the order of 10%, while in Fig. 2(b) the heights, shapes and relative line positions differ for positive and negative detuning. In the following we discuss the reasons for these asymmetries.

In the 5-Gauss case, it is observed that the Rydberg EIT spectrum splits symmetrically into two peaks of approximately equal shape. The corresponding EIT resonance conditions that follow from Eq. (6) correspond to the cascade $|6S_{1/2} F_g = 4, m_{F,g} = 4> \rightarrow |6P_{3/2}F_e = 5, m_{F,e} = 5> \rightarrow |33S_{1/2},m_{J,r} = 1/2, m_I = 7/2>$, labeled A (blue-shifted), and the cascade $|6S_{1/2} F_g = 4, m_{F,g} = -4> \rightarrow |6P_{3/2}F_e = 5, m_{F,e} = -5> \rightarrow |33S_{1/2},m_{J,r} = -1/2, m_I = -7/2>$, labeled A' (red-shifted). The velocities at which the EIT resonances occur are -6.0 m/s (blue-shifted peak, A)

and 6.0 m/s (red-shifted peak, A'). For the velocity class near −6.0 m/s, the σ^+-component of the x-polarized probe field is closer to resonance, leading to optical pumping close the state $m_{F,g} = 4$, which in turn produces the strong blue-shifted EIT peak A, in conjunction with the σ^--component of the x-polarized coupling field. Similarly, for $v \approx +6.0$ m/s the σ^--component of the probe field is closer to resonance, leading to optical pumping close to $m_{F,g} = -4$, which produces the red-shifted peak A', in conjunction with the σ^+-component of the coupling field. Since the optical pumping is not perfect, a small fraction of the atoms reside in $m_{F,g} = \pm 3, \pm 2, \ldots$. Those atoms are driven on the B and B' etc. sequences (see Fig. 1(a)), leading to a slight broadening on the blue side of A and the red side of A'. Without quadratic Zeeman shift, and if the $F_e = 4, 3$ HFS levels were several GHz away from $F_e = 5$, the situation in Fig. 2(a) would exhibit perfect symmetry about $\Delta_C = 0$. The slight asymmetry Fig. 2(a), seen in both the experiment and the simulation, is a first indication that quadratic Zeeman shifts, and possibly other intermediate-state HFS levels, play a role even at small fields. It is somewhat surprising that at fields as small as 5 Gauss there already is evidence for the effects of quadratic Zeeman shifts on EIT spectra. In the 40-Gauss data, shown in Fig. 2(b), the weak satellite peaks, labeled B', C' and B, C, D, are largely resolved and appear outside the interval between A' and A. The satellite peaks are cascades identified by corresponding labels in Fig. 1(a). Both the separations and the strengths of the satellite peaks are highly asymmetric in the 40-Gauss magnetic field. The asymmetry in the positions and the strengths of the satellite peaks increases with magnetic field. It is due to the interplay between optical pumping and the quadratic Zeeman effect for hyperfine states, which introduces the asymmetry in the line splitting and, more importantly, in the optical-pumping efficiency and the resultant relative strengths of the satellite peaks relative to the main (A and A') peaks (see Sec. 4.3).

4.2 EIT line positions and splittings

We have taken a series of data similar to Fig. 2 for a series of magnetic fields. The measured and calculated shifts of the two main EIT peaks, A and A', and of the three blue-shifted satellite peaks, B, C and D, are shown as a function of magnetic field in Fig. 3(a). In the calculations we use Eq. (6) with level shifts $\Delta_g(B)$, $\Delta_e(B)$ and $\Delta_r(B)$ taken from numerical diagonalization of $\hat{H}_{hfs} + \hat{H}_B$ (see Eqs. (2) and 3) within the respective ground-, intermediate- and Rydberg-level subspaces. The larger error bars and the absence of satellite peaks in magnetic fields < 15 Gauss reflect the fact that in such small fields the Zeeman splittings between the satellite lines cannot be experimentally resolved. In Fig. 3(a) it is seen that the two main peaks shift linearly as a function of magnetic field. This is expected because these peaks only involve aligned states, i.e. states with $m_I + m_J = I + J$. Those states have no quadratic Zeeman effect in the magnetic-field range of interest. Close inspection of Fig. 3(a) further reveals that the satellite peaks deviate from the dashed straight lines, which mark the line positions one would observe under absence of quadratic Zeeman shifts. The experimentally observed and calculated deviations of the EIT peaks from the straight lines are in excellent agreement. They are almost entirely due to the quadratic Zeeman effect of the magnetic sublevels of the intermediate ($6P_{3/2}$) state, and they become significant at fields larger than about 20 Gauss. At the largest field in Fig. 3 the nonlinear contribution to the shift of the D-peak approaches 10 MHz, corresponding to about ten times the uncertainty in the experimental line positions. Figure 3(b) shows measured and calculated intervals between the two main peaks divided by the magnetic field, $\Delta\chi_{AA'} = (A − A')/B$, as a function of the line positions A and A' and the magnetic field B. The calculated value for $\Delta\chi_{AA'}$ is fixed at $2\pi \times$ 1.88 MHz/Gauss, while the observed $\Delta\chi_{AA'}$-value approaches the calculated result to within the uncertainty for fields B exceeding about 15 Gauss. The disagreement between the calculated and observed $\Delta\chi_{AA'}$-values seen at small fields is likely due to the fact that in small fields the satellite and main lines are not resolved. In that case, the A, B, C and D lines merge into a single line whose center is blue-shifted relative to the calculated A-line. Likewise, the

A', B' etc. lines merge into a single line that is red-shifted relative to the calculated A'-line. As a result, at small fields the measured $\Delta\chi_{AA'}$-values exceed the calculated ones. In Fig. 3(b) we also show the average splitting between adjacent satellite peaks divided by B, denoted $\Delta\chi_{\text{sat}}$. The measured $\Delta\chi_{\text{sat}}$-value gradually increases from about $2\pi \times 0.25$ MHz/Gauss at 15 Gauss, where the satellite lines start to become resolved, to $2\pi \times 0.28$ MHz/Gauss at 50 Gauss. The calculated $\Delta\chi_{\text{sat}}$-value increases from $2\pi \times 0.21$ MHz/Gauss at zero field to $2\pi \times 0.28$ MHz/Gauss at 50 Gauss; the increase is due to the quadratic Zeeman shift. Considering the EIT linewidth in the experiment, experimental and calculated data in Fig. 3(b) are in good agreement and validate the importance of the quadratic Zeeman effect even in small magnetic fields.
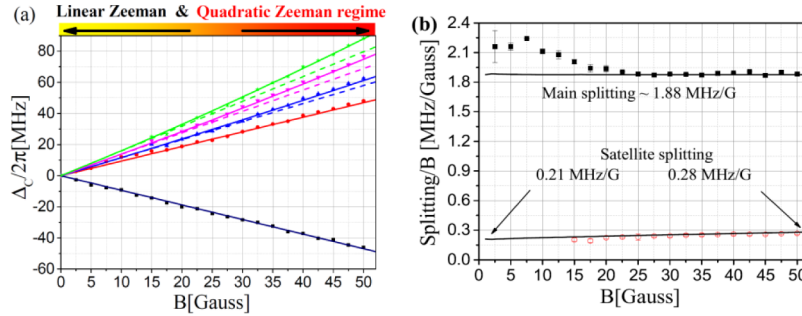

Fig. 3. (a) Experimental (symbols) and calculated (solid lines) frequency shifts of main peaks A' (black squares) and A (red circles), and of the blue-shifted satellite peaks B (blue up triangles), C (pink down triangles) and D (green stars). The dashed lines show line shifts calculated under the assumption of no quadratic Zeeman effect. (b) Line intervals divided by magnetic field for the A'-A interval (black squares), and for the average separations between adjacent lines pairs, A-B, B-C and C-D (red circles), as a function of magnetic field. Symbols show experimental data, solid lines show calculated values that take quadratic Zeeman shifts into account.

4.3 Interplay between optical pumping and EIT

In this section we discuss optical-pumping effects and their relation with EIT. In optical pumping [35], the distribution of atomic populations over the Zeeman sublevels becomes non-thermal after several absorption emission cycles. Without magnetic field and for zero velocity atoms, probe light that is linearly polarized along x optically pumps atoms mostly into the states $|6S_{1/2}, F = 4, m_{F,g} = \pm 4>$, implying a symmetric situation in which the A and A' probe transitions in Fig. 1 account for most absorption. The optical pumping is reduced when the degeneracy of the Zeeman transitions is lifted. Under presence of a magnetic field pointing along z, the transitions driven by the σ^+- and σ^--components of the x-polarized probe field become detuned from one another, due to the different g_F -factors of the $6S_{1/2}$ and $6P_{3/2}$ states. In this case, optical pumping primarily occurs for combinations of atom velocities and probe detuning for which either the A or the A' probe transition is near-resonant (but not both). This is illustrated by simulation results in Fig. 4 under a magnetic field of 40 Gauss and $\Delta_P = 0$. As seen from Eq. (6), for fixed Δ_P the free parameters available to achieve the EIT resonance condition on both the probe and the coupling transitions are the atom velocity v in the z direction and the coupling detuning Δ_C. The range of available velocity classes to satisfy the conditions follow from the Maxwellian density distribution of thermal atoms, $N(v) = N_0 / (u\sqrt{\pi})\exp(-v^2 / u^2)$, where $u / \sqrt{2}$ is the root-mean-square atomic velocity in one dimension. Here, $u / \sqrt{2} \approx 140$ m/s, N_0 denotes the total atomic volume density in the cell, and $N(v)$ is the velocity-dependent volume density per m/s. According to Eq. (6), the resonant velocities only depend on Δ_P, which is zero in the simulation, and on the ground- and intermediate-level Zeeman shifts (notably not on Δ_C). In Fig. 4, the A-transition is near-

resonant for atoms with velocities $v \approx$ –48 m/s. This leads to optical pumping to near $<m_I + m_J$ $>$ = 4, as shown in the middle and right panels in Fig. 4, as well as high photon scattering rates for atoms in this velocity class, as seen in the left panel in Fig. 4. Similarly, the A′-transition is near-resonant for atoms with velocities $v \approx$ 48 m/s, leading to optical pumping to near $<m_I + m_J> $ = –4 and high photon scattering rates for atoms in that velocity class. The left panel in Fig. 4 further shows that atoms near those velocities account for most absorption, independent of Δ_C. Atoms with velocities between –48 m/s and 48 m/s are optically pumped to some intermediate value of $<m_I + m_J>$. However, these atoms have lower photon scattering rates, and they contribute little to the overall absorption behavior. For completeness we note that in our magnetic-field range the resonant velocities are much smaller than the root-mean-square atomic velocity. Therefore, the density reduction in $N(v)$ due to the Maxwell distribution is only on the order of 5% and has no significant effect on the spectra.
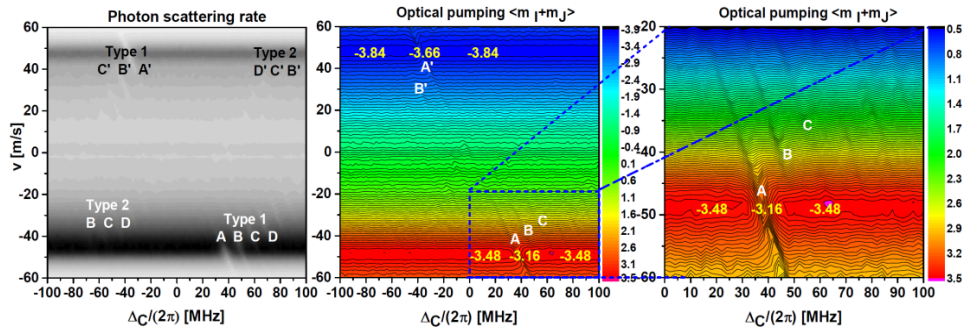

Fig. 4. Left: simulated photon scattering rate vs coupling detuning and atom velocity for 40 Gauss magnetic field in x-polarized coupling and probe fields with respective radial Rabi frequencies $\Omega_{C,r}/(2\pi)$ = 8 MHz and $\Omega_{P,r}/(2\pi)$ = 2 MHz, on a linear gray scale ranging from 0 (white) to 2.8 × 10^6 s^{-1} (black) per atom. The labels of the features visible in the plot correspond with the labels Fig. 1. Middle and right (zoom-in): simulated expectation values for the ground-state $< m_I + m_J >$, obtained from the same simulation as on the left, on color scales given by the color bars. Regions of strong photon scattering correspond with fairly efficient optical pumping into the aligned states, $|m_{F,g} = \pm 4>$. In the regions of large photon scattering the Zeeman shifts of the probe cycling transitions, $|m_{F,g} = \pm 4> \rightarrow |m_{F,e} = \pm 5>$, are compensated by the Doppler effect at $v \approx \mp$ 48 m/s. The numbers indicated on the figures show the approximate values of $<m_I + m_J>$ on the main EIT resonances, A and A', and close to them. It is seen that the EIT-induced reduction in probe photon scattering is accompanied by a reduction in optical-pumping efficiency. The plots also show a significant asymmetry between positive and negative v, and between positive and negative Δ_C.

Further inspection of Fig. 4 shows an asymmetry between positive and negative velocities, as well as in the degree to which the $<m_I + m_J>$-values approach the limits ± 4 (corresponding to perfect optical pumping into the aligned states, which have $m_I + m_J = \pm (I + J)$). The asymmetry is a result of the quadratic Zeeman effect in the $6P_{3/2}$ state. The levels $m_I + m_J = 5, 4, 3...$ are considerably more closely spaced than the levels $m_I + m_J = -5, -4, -3...$ (see, for instance, in [27]). Hence, the $m_I + m_J = 5, 4, 3...$ Zeeman splittings in $6P_{3/2}$ match the splittings of the $m_I + m_J = 4, 3, 2...$ in the ground state $6S_{1/2}$ much more closely than the $m_I + m_J = -5, -4, -3...$ splittings in $6P_{3/2}$ match the splittings of the $m_I + m_J = -4, -3, -2...$ in $6S_{1/2}$. This leads to higher photon scattering rates at $v \approx$–48 m/s. In the middle and right panels of Fig. 4 we indicate the extremal values of $<m_I + m_J>$. At coupling detuning away from the EIT features, the $<m_I + m_J>$-values peak at −3.84 (lower photon scattering, $v \approx$ 48 m/s) and 3.48 (higher photon scattering, $v \approx$–48 m/s). It is therefore seen that higher scattering rates correspond with somewhat less efficient pumping. In the EIT signals, the less efficient optical pumping at $v \approx$–48 m/s leads to quite pronounced satellite peaks B, C and D on the blue side of peak A, at $\Delta_C \sim 2\pi \times$ 50 MHz. From Figs. 1-4 it is evident that the peak A corresponds with $m_{F,g}$ = 4, B corresponds with $m_{F,g}$ = 3 etc. Hence, the incomplete optical pumping into

$m_{F,g} = 4$ causes the relatively strong B, C and D satellite peaks. Conversely, the more efficient optical pumping at $v \approx +48$ m/s into $m_{F,g} = -4$ leads to less pronounced satellite peaks B′ and C′ on the red side of peak A′, at $\Delta_C \sim -2\pi \times 50$ MHz in the EIT spectrum.

It is further noteworthy that away from the EIT resonances the coupling beam has very little effect on optical pumping behavior. This reflects the fact that away from the EIT resonances there is no velocity- detuning pair (v, Δ_C) that satisfies an EIT double-resonance for both coupling and probe fields. However, on the EIT resonances the coupling inhibits probe-photon scattering, leading to substantial drops in photon scattering and optical-pumping efficiency. For instance, the EIT peak labeled A reduces $<m_I + m_J>$ from about 3.48 to 3.16, and the EIT peak labeled A′ reduces $|<m_I + m_J>|$ from about 3.84 to 3.66. The corresponding "grooves" in the photon-scattering and optical-pumping maps are clearly seen in Fig. 4.

In simulations not shown, the asymmetry trends seen in Figs. 2 and 4, as well as the back-action of EIT onto optical pumping, have also been observed at other magnetic fields. In these studies it is confirmed that the asymmetries in photon scattering and optical pumping, seen between positive and negative coupling detuning Δ_C and velocities v, are due to the nonlinear Zeeman effect and generally increase with magnetic field. Asymmetry already becomes evident at fields as small as about 5 Gauss; in lesser fields the nonlinear Zeeman effect is so small that spectra, photon-scattering and optical-pumping maps are essentially symmetric in Δ_C and v. At small fields below about 15 Gauss, the quadratic Zeeman shifts mostly manifest as an asymmetry in the line heights that traces back to an asymmetry in optical pumping (which is due to quadratic Zeeman shifts that are too small to be observed in line positions). At higher fields, the quadratic Zeeman shifts can also be directly seen in an asymmetry in line positions and splittings.
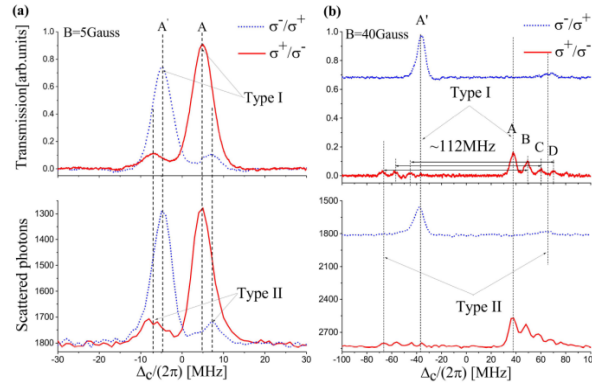

Fig. 5. Experimental (top) and calculated (bottom) Rydberg EIT spectra in 852 σ^+/ 510 σ^- and 852 σ^-/ 510 σ^+ polarized probe and coupling fields. The magnetic fields are 5 Gauss (a) and 40 Gauss (b). The EIT spectra in (a) are approximately symmetric about $\Delta_C = 0$, while they are highly asymmetric in shape and background absorption in Fig. 5(b). The asymmetry is due to the quadratic Zeeman effect of the intermediate $6P_{3/2}$ level. The line labels and types are explained in Fig. 1 and in the text.

4.4 Optical-pumping effects on EIT for other polarizations

We have also observed asymmetry of Rydberg EIT spectra in a series of analogous experiments for polarization cases 852 σ^+/ 510 σ^- and 852σ^- / 510 σ^+. The experimental results and corresponding simulations are shown in the top and bottom panels in Fig. 5, respectively. When the magnetic field is only 5 Gauss, the Rydberg EIT spectra are almost symmetric about Δ_C because in fields that small there is no significant quadratic Zeeman effect. In contrast, at 40 Gauss the Rydberg EIT spectra for the two polarization cases in Fig. 5 are highly asymmetric, in a way that closely resembles the asymmetry seen in Fig. 2.

Especially, there are three clear satellite peaks, B, C and D, on the blue side of A, while there are no significant satellite peaks, B' etc, on the red side of A′. The increase in asymmetry at larger magnetic fields reflects the increasing importance of the quadratic Zeeman effect in those fields.

It is also noted that the quadratic Zeeman effect brings about an asymmetry in overall background absorption. At 5 Gauss the absorption away from the EIT peaks is almost the same for σ^+- and σ^--polarized probe fields, while at 40 Gauss the σ^+-polarized probe is considerably more absorbed than the σ^--polarized probe. Note the corresponding difference in the number of scattered photons in the simulations (bottom panels in Fig. 5). Another interesting observation in the 40-Gauss data in Fig. 5 is the clear appearance of the "Type-II"-peaks. As seen in Fig. 1(a), the "Type-II"-transitions, shown by dashed green arrows, have much lower Rabi frequencies than the dominant "Type-I"-transitions (solid green arrows).

The difference in Rabi frequencies is mostly caused by the different sizes of the inner products between the electron-spin parts of the intermediate and the Rydberg states; the "Type II"-transitions tend to flip the spin. Since the Rydberg state is in the deep hyperfine Paschen-Back regime, the frequency shift between corresponding Type-I and Type-II lines is $B \times 2.8$ MHz/Gauss, corresponding to 112 MHz in the right panels in Fig. 5 (see horizontal arrows).

5. Conclusion

We have performed Rydberg EIT spectroscopy in a cesium room-temperature vapor cell when an axial magnetic field in the range between 0 and 50 Gauss is applied. The Rydberg EIT spectra exhibit characteristic sets of peaks and satellite lines that become noticeably asymmetric at fields as low as 5 Gauss, and highly asymmetric in fields of ~ 40 Gauss and above. We have modeled the spectra using Quantum Monte Carlo wave-function simulations. The EIT spectra were found to be quite susceptible to the quadratic Zeeman effect, which leads to considerable asymmetry in both the line splittings and the line strengths and shapes of the red-detuned versus the blue-detuned Zeeman features of the EIT lines. The simulations also showed that the asymmetry in EIT satellite line strengths is, in large parts, due to differences in the optical-pumping efficiency on the red versus the blue shifted parts of the spectra. The presented results are a prerequisite for spectroscopic, EIT-based diagnostics that involve a background magnetic field in the tens to hundreds of Gauss range. In this regime, optical pumping rates are reduced in comparison with field-free conditions, but they are still high enough to affect EIT spectra. Moreover, there is a cross talk between EIT and optical pumping that must be modeled for a quantitative interpretation of spectroscopic results. At lower magnetic fields, optical pumping rates are not reduced by Zeeman detunings and approach the field-free case, while at higher fields optical pumping tends to become ineffective. Our work addresses applications in the intermediate magnetic-field regime of tens to hundreds of Gauss, which can benefit from a detailed modeling. As an example, in a recent study the electric fields in magnetized plasma have been characterized using Rydberg EIT and electric-field-induced Stark shifts of Rydberg levels [28]. This study has already benefited from the insights obtained in the present work. Atom-based electric-field diagnostics using Rydberg EIT in magnetized plasma may also apply to other technical implementations, such as process plasma, Hall thruster etc.

Funding

References

1. T. F. Gallagher, *Rydberg Atoms* (Cambridge University,2008).
2. D. Jaksch, J. I. Cirac, P. Zoller, S. L. Rolston, R. Côté, and M. D. Lukin, "Fast quantum gates for neutral atoms," Phys. Rev. Lett. **85**(10), 2208–2211 (2000).
3. E. Urban, T. A. Johnson, T. Henage, L. Isenhower, D. D. Yavuz, T. G. Walker, and M. Saffman, "Observation of Rydberg blockade between two atoms," Nat. Phys. **5**(2), 110–114 (2009).
4. Y. O. Dudin and A. Kuzmich, "Strongly interacting Rydberg excitations of a cold atomic gas," Science **336**(6083), 887–889 (2012).
5. T. Peyronel, O. Firstenberg, Q.-Y. Liang, S. Hofferberth, A. V. Gorshkov, T. Pohl, M. D. Lukin, and V. Vuletić, "Quantum nonlinear optics with single photons enabled by strongly interacting atoms," Nature **488**(7409), 57–60 (2012).
6. S. Diehl, A. Tomadin, A. Micheli, R. Fazio, and P. Zoller, "Dynamical phase transitions and instabilities in open atomic many-body systems," Phys. Rev. Lett. **105**(1), 015702 (2010).
7. C. Carr, R. Ritter, C. G. Wade, C. S. Adams, and K. J. Weatherill, "Nonequilibrium phase transition in a dilute Rydberg ensemble," Phys. Rev. Lett. **111**(11), 113901 (2013).
8. M. Marcuzzi, E. Levi, S. Diehl, J. P. Garrahan, and I. Lesanovsky, "Universal nonequilibrium properties of dissipative Rydberg gases," Phys. Rev. Lett. **113**(21), 210401 (2014).
9. M. L. Zimmerman, J. C. Castro, and D. Kleppner, "Diamagnetic structure of Na Rydberg states," Phys. Rev. Lett. **40**(16), 1083–1086 (1978).
10. J. Sedlacek, A. Schwettmann, H. Kübler, R. Löw, T. Pfau, and J. P. Shaffer, "Microwave electrometry with Rydberg atoms in a vapour cell using bright atomic resonances," Nat. Phys. **8**(11), 819–824 (2012).
11. S. Harris, "Electromagnetically induced transparency," Phys. Today **50**(7), 36–42 (1997).
12. A. K. Mohapatra, T. R. Jackson, and C. S. Adams, "Coherent optical detection of highly excited Rydberg states using electromagnetically induced transparency," Phys. Rev. Lett. **98**(11), 113003 (2007).
13. A. K. Mohapatra, M. G. Bason, B. Butscher, K. J. Weatherill, and C. S. Adams, "A giant electro-optic effect using polarizable dark states," Nat. Phys. **4**(11), 890–894 (2008).
14. C. Wade, M. Marcuzzi, E. Levi, J. M. Kondo, I. Lesanovsky, C. S. Adams, and K. J. Weatherill, "Terahertz-driven phase transition applied as a room-temperature terahertz detector," https://arXiv:1709.00262 (2017).
15. J. A. Sedlacek, A. Schwettmann, H. Kübler, and J. P. Shaffer, "Atom-based vector microwave electrometry using rubidium Rydberg atoms in a vapor cell," Phys. Rev. Lett. **111**(6), 063001 (2013).
16. S. X. Bao, H. Zhang, J. Zhou, L. J. Zhang, J. M. Zhao, L. T. Xiao, and S. T. Jia, "Polarization spectra of Zeeman sublevels in Rydberg electromagnetically induced transparency," Phys. Rev. A **94**(4), 043822 (2016).
17. D. J. Fulton, S. Shepherd, R. R. Moseley, B. D. Sinclair, and M. H. Dunn, "Continuous-wave electromagnetically induced transparency: A comparison of V, Λ, and cascade systems," Phys. Rev. A **52**(3), 2302–2311 (1995).
18. C. Y. Ye and A. S. Zibrov, "Width of the electromagnetically induced transparency resonance in atomic vapor," Phys. Rev. A **65**(2), 023806 (2002).
19. H. S. Moon and H. R. Noh, "Optical pumping effects in ladder-type electromagnetically induced transparency of $5S_{1/2}$–$5P_{3/2}$–$5D_{3/2}$ transition of ^{87}Rb atoms," J. Phys. At. Mol. Opt. Phys. **44**(5), 055004 (2011).
20. Z. S. He, J. H. Tsai, Y. Y. Chang, C. C. Liao, and C. C. Tsai, "Ladder-type electromagnetically induced transparency with optical pumping effect," Phys. Rev. A **87**(3), 033402 (2013).
21. S. M. Rochester, K. Szymański, M. Raizen, S. Pustelny, M. Auzinsh, and D. Budker, "Efficient polarization of high-angular-momentum systems," Phys. Rev. A **94**(4), 043416 (2016).
22. A. E. Mironov, J. D. Hewitt, and J. G. Eden, "Spin polarization of Rb and Cs np ^{2}P$_{3/2}$ (n=5, 6) atoms by circularly polarized photoexcitation of a transient diatomic molecule," Phys. Rev. Lett. **118**(11), 113201 (2017).
23. L. Ma, D. A. Anderson, and G. Raithel, "Paschen-Back effect and Rydberg-state diamagnetism in vapor-cell electromagnetically induced transparency," Phys. Rev. A **95**(6), 061804 (2017).
24. V. Bendkowsky, B. Butscher, J. Nipper, J. P. Shaffer, R. Löw, and T. Pfau, "Observation of ultralong-range Rydberg molecules," Nature **458**(7241), 1005–1008 (2009).
25. F. Böttcher, A. Gaj, K. M. Westphal, M. Schlagmüller, K. S. Kleinbach, R. Löw, T. C. Liebisch, T. Pfau, and S. Hofferberth, "Observation of mixed singlet-triplet Rb₂ Rydberg molecules," Phys. Rev. A **93**(3), 032512 (2016).
26. M. Xiao, Y. Li, S. Jin, and J. Gea-Banacloche, "Measurement of dispersive properties of electromagnetically induced transparency in rubidium atoms," Phys. Rev. Lett. **74**(5), 666 (1995).
27. Y. C. Jiao, X. X. Han, Z. W. Yang, J. K. Li, G. Raithel, J. M. Zhao, and S. T. Jia, "Spectroscopy of cesium Rydberg atoms in strong radio-frequency fields," Phys. Rev. A (Coll. Park) **94**(2), 023832 (2016).
28. D. Staack, Y. Raitses, and N. J. Fisch, "Shielded electrostatic probe for nonperturbing plasma measurements in hall thrusters," Rev. Sci. Instrum. **75**(2), 393–399 (2004).
29. D. Anderson, G. Raithel, M. Simons, and C. L. Holloway, "Quantum-optical spectroscopy for plasma electric field measurements and diagnostics," https://arXiv:1712.08717 (2017).
30. D. A. Steck, Cesium D Line Data, available online at http://steck.us/alkalidata (2010), pp. 9–10.
31. H. Saßmannshausen, F. Merkt, and J. Deiglmayr, "High-resolution spectroscopy of Rydberg states in an ultracold cesium gas," Phys. Rev. A **87**(3), 032519 (2013).
32. K. Mølmer, Y. Castin, and J. Dalibard, "Monte Carlo wave-function method in quantum optics," J. Opt. Soc. Am. B **10**(3), 524–538 (1993).

33. J. Dalibard, Y. Castin, and K. Mølmer, "Wave-function approach to dissipative processes in quantum optics," Phys. Rev. Lett. **68**(5), 580–583 (1992).
34. N. V. Morrow and G. Raithel, Advances in Atomic, Molecular and Optical Physics **53**, 187–225, eds. M. Scully and G. Rempe (Elsevier, 2006).
35. W. Happer, "Optical Pumping," Rev. Mod. Phys. **44**(2), 169–249 (1972).